

Optical investigations on the mobility of two-dimensional excitons in GaAs/Ga_{1-x}Al_xAs quantum wells

H. Hillmer, A. Forchel, S. Hansmann, M. Morohashi,* and E. Lopez

4. Physikalisches Institut, Universität Stuttgart, D-7000 Stuttgart-80, Pfaffenwaldring 57, Federal Republic of Germany

H. P. Meier

IBM Research Division, Zürich Research Laboratory, CH-8803 Rüschlikon, Switzerland

K. Ploog

Max-Planck-Institut für Festkörperforschung, D-7000 Stuttgart-80, Heisenbergstrasse 1, Federal Republic of Germany

(Received 16 December 1988)

By time-of-flight studies, the lateral transport of two-dimensional excitons in GaAs/Ga_{1-x}Al_xAs quantum wells is studied with a very high spatial resolution ($\sim 0.1 \mu\text{m}$) provided by laterally microstructured masks. The motion of the excitons is investigated for different quantum-well widths over a wide temperature range and can be described entirely by isothermal diffusion. In particular, at low temperatures the diffusivity strongly decreases with decreasing well width. The low-temperature mobilities are found to be mainly determined by interface-roughness scattering. In the range where acoustic-deformation-potential scattering is dominant, the mobility of the excitons as a function of temperature and well width is found to agree with the corresponding theoretical mobility limits. The excitonic scattering condition describes the experiment much better than the ambipolar scattering condition. The comparison of experimental results and calculated mobility limits shows that barrier-alloy disorder scattering significantly affects the mobilities of excitons only in narrow GaAs/Ga_{1-x}Al_xAs quantum wells.

I. INTRODUCTION

Since the first report of two-dimensional (2D) conduction in III-V semiconductor heterostructures, extensive experimental and theoretical studies have focused on the various transport properties. Hall measurements have been used repeatedly. In most of these studies the mobility increase in single heterojunctions due to modulation doping¹⁻⁵ has been examined, while fewer publications report on measurements in modulation-doped quantum-well (QW) structures⁶ and in undoped QW's.^{7,8} Time-of-flight (TOF) techniques are used rarely, although they allow the determination of mobilities directly. In electro-optical TOF measurements, carriers are generated at a desired sample position by short laser pulses. The laser can be positioned by an optical lens⁹ or by a fiber.¹⁰ In the external field the generated carriers move to electric contacts^{9,11} or a *p-n* junction¹⁰ in a known distance (flight distance). The actual position of the carriers can further be detected by an imaging method, as used by Höpfel *et al.*¹² for 2D minority-carrier-mobility studies in GaAs/Ga_{1-x}Al_xAs. In a MOSFET-like device (MOSFET denotes metal-oxide-semiconductor field-effect transistor), minority-carrier mobilities were obtained by TOF studies for the first time by Nelson *et al.*¹¹ In all these unipolar TOF studies, minority-carrier mobilities are obtained, and, except for Ref. 11, the spatial resolution is given by the positioning accuracy of the laser.

The ambipolar transport, in contrast, which is deter-

mined by the motion of an electron-hole cloud, has been the subject of few investigations. The perpendicular transport in graded GaAs/Ga_{1-x}Al_xAs superlattices was investigated by TOF luminescence spectroscopy.¹³ The motion of 2D excitons in GaAs QW's (Ref. 14) was studied in the low-temperature range by the method of transient gratings. This method was also used for studies of 2D diffusivities in Si:H and SiC:H.¹⁵ In GaAs QW's the motion of a 2D electron-hole plasma was studied by TOF measurements¹⁶ with a high spatial resolution yielding a diffusive motion of the plasma. This is in contradiction to strong drift effects inferred from time-resolved Raman scattering,¹⁷ carried out with low spatial resolution.

In this paper the 2D exciton transport is studied by TOF measurements, which have been optimized to achieve a high spatial resolution. In Sec. II we present an outline of the experimental method emphasizing the mask technique and the laser-spot positioning used to obtain a very high spatial resolution. Time-integrated and time-resolved photoluminescence spectra of masked and unmasked samples are discussed in Sec. III. A theoretical description for the transport measurements based on the 2D diffusion equation is given in Sec. IV. Section V deals with transport properties like diffusivities and mobilities, obtained by line-shape fits from the experiment. The mobility as a function of temperature and well width will be described by different scattering mechanisms in Sec. VI. Finally, concluding remarks are given in Sec. VII. Preliminary results of our work have been published elsewhere.¹⁸

II. PRINCIPLES OF THE TIME-OF-FLIGHT METHOD

Time-of-flight experiments are based on the detection of carrier motion as a function of spatial position and time. In ambipolar transport experiments, the radiative recombination, which is proportional to the carrier concentration if the latter is not too high, represents an excellent access to probe the carrier motion. This was demonstrated recently in a number of vertical and lateral TOF studies^{13,16,18–20} and for different material systems.

To study the lateral motion of free excitons by optical spectroscopy, we use a sample mask combination which is shown schematically in Fig. 1. The transport distances are defined by microstructured masks which are placed directly on the heterostructure surface. We have used NiCr layers (thickness 200 nm) on thin glass substrates to define the masks. By optical lithography and dry etching, circular areas (holes) of different radii R (0.5–100 μm) are etched into the NiCr as the only areas which are transmittive for both the excitation light from the laser and the luminescence of the sample. By short, weak laser pulses (solid-line arrows), excitons are generated in the GaAs quantum well (QW) inside one of the circular areas defined by the mask. The position of the exciton cloud is displayed in Fig. 1 for $t=0$ by the black area. Recording the emission of the QW (dashed-line arrows) as a function of time, the evolution of the exciton concentration in the area defined by the hole can be directly observed. Those excitons moving under masked parts during their lifetime do not contribute to the detectable emission. Therefore, the time-resolved emission from the hole area includes information on important transport properties like the diffusivity and the mobility, which can be extracted by the evaluation of these profiles as a function of both temperature and well width.

Figure 2 depicts the experimental setup used for the lateral TOF studies. The beam of a synchronously mode-locked dye laser (~ 8 ps, 615 nm) is expanded and spatial-

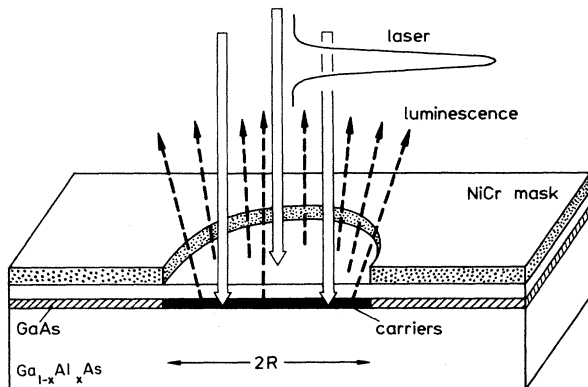


FIG. 1. Schematic design of the sample-mask combination used to obtain a high lateral resolution. By short laser pulses (solid lines) a carrier cloud is generated inside the single QW. The radiative recombination (dashed-line arrows) is detected time resolved and used to probe the exciton concentration remaining under the hole area.

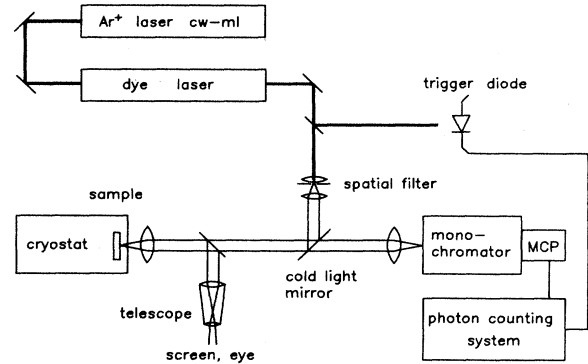


FIG. 2. Design of the experimental setup. Pulses from a synchronously mode-locked laser are focused on the sample with a spot radius of 15 μm . The position of the spot is carefully controlled via a microscope-like observation setup (objective, telescope).

ly filtered. The beam is deflected by a heat-transmitting mirror (cold light mirror, onset wavelength 700 nm) and focused by a microscope objective on the sample-mask combination, which is mounted on a cold finger of a variable-temperature cryostat (10–300 K). The position and size of the laser spot on the mask are controlled very carefully via a telescope. The smallest spot diameter which can be obtained with this method is 1 μm and agrees with the theoretical limit for this wavelength and beam waist. This small focus was used in our previous lateral TOF studies of 2D electron-hole plasma transport.¹⁶ In the TOF studies of exciton transport reported here, a laser spot of 15 μm was carefully maintained. The laser spot and the laser power were chosen appropriately to obtain sufficiently low excitation densities for free-exciton formation. The luminescence of the sample is collected by the same objective which is used for focusing the laser, passes the cold light mirror, and is dispersed by a monochromator. The signal is detected via a fast photon-counting system using a microchannel plate photomultiplier, which yields a total time resolution of about 50 ps.

Our method enables us to study carrier transport in lateral direction with an ultrahigh spatial resolution (~ 0.1 μm) given by the masks. Previous TOF methods were often limited by the laser-spot size and the positioning accuracy of the spot.^{9,10,12,17} The generated carrier system has a radial symmetry because of the symmetry of the fundamental mode of the laser (TEM_{00}). The highest sensitivity for lateral TOF studies is therefore obtained for the radial transport geometries used in this paper and elsewhere.^{16,18}

TABLE I. This table gives the layer thickness and composition of the samples investigated. L_z is the width of the GaAs quantum well, L_B the thickness of the $\text{Ga}_{1-x}\text{Al}_x\text{As}$ barrier, and x_{Al} the aluminum mole fraction of the barrier.

| Sample no. | L_z (nm) | L_B (nm) | x_{Al} |
|------------|------------|------------|-----------------|
| 1 | 4,8,15 | 35,50 | 0.5 |
| 2 | 74 | 20 | 1 |

III. EXPERIMENTAL RESULTS

Since the radiative recombination is used to probe the carrier concentration, the first part of this section deals with time-integrated and time-resolved photoluminescence studies on the GaAs/Ga_{1-x}Al_xAs samples as a function of temperature, well width, and excitation power. The second part demonstrates how qualitative information about the transport can be derived directly from the measured profiles.

The samples used for our experiments contain different single QW's and are grown by molecular-beam epitaxy (MBE) on GaAs substrates. Details on the sample structures are summarized in Table I. Sample 1 includes QW's of different well width L_z , which implies identical growth and mask conditions for these QW's. The time-integrated photoluminescence (Fig. 3) shows the emissions of the three single QW's and of the substrate. The time-integrated studies are carried out under the same experimental conditions as the time-resolved studies using the pulsed laser system. The excitation energy of the laser (2.01 eV) leads to a creation of electron-hole pairs only inside the QW's. For peak excitation densities below 100 kW/cm², the QW emissions show a constant linewidth and a monoexponential decay. We observe no excitation-intensity dependence of the lifetime for excitation intensities in this range. All measurements reported in the following are carried out with peak excitation intensities of 50 kW/cm², which creates a carrier density of about 5×10^{15} cm⁻³. As shown below, this leads to a formation of excitons, especially for low temperatures.

The carrier lifetime and, in particular, its dependence on the well width L_z and the temperature are essential for the evaluations explained below. Figure 4 depicts the lifetime as a function of temperature for three different well widths. The lifetimes start at helium temperatures at relative small values of a few hundred ps and increase with rising temperature to values in the order of 3 ns. At still higher temperatures ($T > 110$ K, e.g., for the QW of 8 nm well width) the lifetime again decreases. For a constant low temperature the lifetimes grow with increasing well width. This dependence of the lifetime on well width and temperature was reported and discussed previously

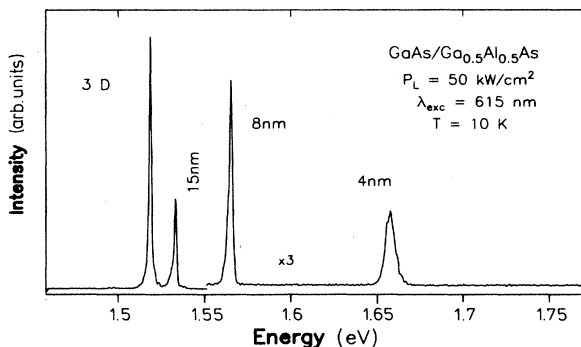


FIG. 3. Time-integrated photoluminescence of a GaAs/Ga_{0.5}Al_{0.5}As sample including QW's of 4, 8, and 15 nm well width.

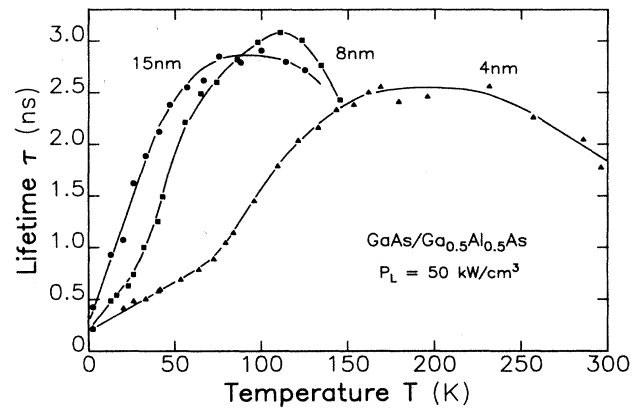


FIG. 4. QW lifetimes of the 4-, 8-, and 15-nm QW's as a function of temperature.

by Feldmann *et al.*,²¹ where QW samples with an aluminum mole fraction of 0.3 were studied in the low-temperature range (2–60 K). In Ref. 21 localization in momentum space and in real space were inferred to explain the lifetime variation with temperature and well width, respectively. In addition to the processes which determine the lifetime at low temperature, the high-temperature behavior is influenced by additional processes like occupation of higher bands, interface recombination, thermal dissociation of the excitons, and polar-optical scattering processes.

Our TOF method is demonstrated in Fig. 5, displaying the emission of a QW with a well width of 15 nm through a mask with holes of different radii as a function of time. The intensity decay time is found to decrease strongly with decreasing hole radius. For large holes ($R \geq 25 \mu\text{m}$), the decay of the QW emission is exponential with a lifetime as measured for unmasked samples (Fig. 4). In this condition, all excitons excited by the laser recombine inside the uncovered area (hole) and the exciton motion does not influence the profiles. With increasing radius, the time-resolved emission is found to decay significantly

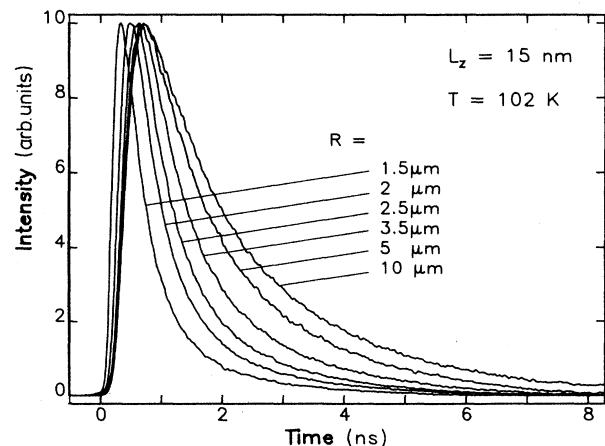


FIG. 5. Experimental transport profiles for a QW with a well width of 15 nm measured for various hole radii R at $T = 102$ K.

faster. This indicates that some excitons can reach covered parts of the structure during their lifetime and do not contribute to the luminescence detected through the hole. Hence, the smaller the radius and the faster the motion, the faster the QW emission decays.

In addition to the information about transport properties which is included in the decay behavior of the exciton emission as mentioned above, the rise of the profiles is determined by the carrier cooling and the exciton-formation time and transport processes if they are relevant on this time scale. Since the excitation energy of the carriers exceeds the energy of the QW ground state, the rise of $n = 1$ emission is expected to be finite even if the time resolution would be theoretically zero. These problems will be discussed in more detail in the next section.

Figure 6 presents an overview of the time-resolved emissions of QW's with three different widths at two different temperatures. In this figure, experimental profiles from uncovered samples (dashed lines) are shown together with profiles measured through a mask hole of $2 \mu\text{m}$ radius (solid line). For the unmasked samples, the time variation is determined by the corresponding lifetime, while the profiles of masked samples show the influence of carrier transport. Comparing these profiles, the qualitative dependence of lateral transport on the well width and temperature can be seen directly. The difference between corresponding profile pairs, e.g., increases with increasing well width. This indicates a faster motion of increasing L_z . Hence, the 2D transport will be characterized by L_z -dependent scattering processes. Furthermore, the excitons are seen to move for larger distances with increasing temperature for two temperatures compared here.

The use of samples containing single QW's of different thickness (e.g., sample 1 in Fig. 6) has the advantage of comparable growth conditions for the wells. However, it must be verified that the different QW's do not influence each other in the transport behavior. Removing the 4-

and 8-nm QW's by etching, we found no change in the transport profiles of the 15-nm QW. Hence, the excitation of QW's with low quantization energy (wide wells) by those of high quantization energy (narrow wells) is negligible compared to the direct laser excitation. Using the respective absorption coefficient, we estimate the order of the optical excitation by the high energetic emission of other QW's to be below 1% of the direct laser excitation of the QW.

IV. THEORETICAL TRANSPORT PROFILES

In this section a transport model is presented to evaluate the time-resolved luminescence from the uncovered sample parts (circular areas). Due to the ambipolar condition (no external field), the continuity equation in the 2D space x, y is transformed into the diffusion equation for the ambipolar concentration c . This equation is supplemented by a linear recombination term including the radiative lifetime τ :

$$\frac{\partial c}{\partial t} = D \left[\frac{\partial^2 c}{\partial x^2} + \frac{\partial^2 c}{\partial y^2} \right] - \frac{c}{\tau}. \quad (1)$$

Using the finite-difference method, this equation is solved numerically with respect to the initial condition. At $t=0$, the concentration profile is given by the laser profile [Gaussian type, full width at half maximum (FWHM) $15 \mu\text{m}$] cut off by the mask geometry. Since the lifetime τ is measured separately, the diffusivity D is the only free parameter in Eq. (1). The intensity of the radiative emission, $I(x, y)$, measured in this TOF experiment is proportional to the concentration $c(x, y)$ because the emission is caused by the recombination of free excitons created by the low excitation intensities used here. As mentioned above, an effective relaxation time has to be taken into account combining the carrier cooling and the exciton-formation time. This is described in a simple

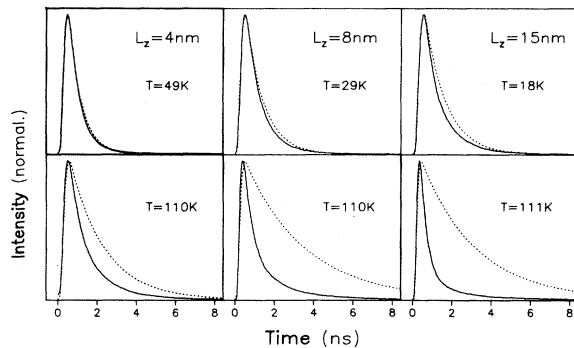


FIG. 6. Experimental transport profiles (solid lines) obtained by recording the emission of different QW's through a mask hole of $R = 2 \mu\text{m}$ radius as a function of time. Corresponding profiles measured without the mask are given by the dashed lines. The difference between correlated pairs is due to the influence of transport. Top row: low-temperature regime. Bottom row: $T = 110 \text{ K}$.

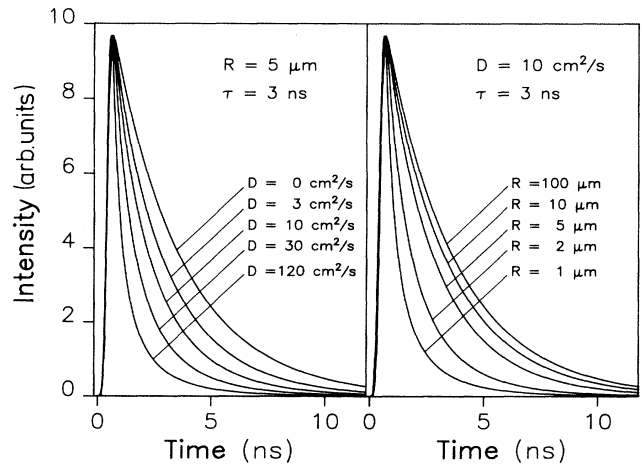


FIG. 7. Theoretical transport profiles calculated for a constant hole radius R and various diffusivities D (left part) for a constant diffusivity and different radii (right part).

three-level model. The first level is populated by the laser and feeds the second level (quantum-well band edge). This process can be described by an effective relaxation time. The third level is populated by recombination processes, which define the lifetime. Note that the effective relaxation time only influences the rise of the profiles, due to the time scales involved here. The experimental time resolution can further be included using a convolution.

To demonstrate the sensitivity of our method some calculated profiles are shown in Fig. 7. The left part depicts concentration profiles with fixed hole radius R for different values of the diffusivity D calculated for a lifetime of 3 ns. For $D=0$ there is no exciton motion in the lateral direction. All excitons excited by the laser recombine inside the hole area; hence the concentration as a function of time represents the exponential decay connected with the lifetime. With increasing D an increasing number of excitons can reach covered sample parts and do not contribute to the recombination signal of the hole area. Hence, the profiles drop faster the higher D is. The right part displays profiles for different values of the hole radius for a fixed diffusivity. For large holes ($R \geq 25 \mu\text{m}$) the influence of exciton diffusion on the profiles is negligible. If the radius is reduced, an increasing number of excitons reaches covered parts during their lifetime and cannot contribute to the emission detected through the hole.

As will be shown now, our method can also be applied to the study of lateral transport of 3D carriers. If the method enables the detection of recombination processes exclusively from a cylindrical volume (the cylinder radius is given by the hole radius), the 3D diffusion equation can be separated into a 2D diffusion equation (lateral transport in x,y direction) and an equation depending only on z (vertical transport). This condition is fulfilled in QW samples, when the QW's are located close to the surface. Further, it is fulfilled in some 3D carrier systems when they remain in a pancakelike shape during the whole transport. Suitable 3D samples therefore confine the carriers in z direction but cause no quantization effects. In our 3D samples this confinement is provided by AlAs barriers which contain a 3D GaAs layer (thickness, e.g., 74 nm).

The theoretical transport profiles shown in Fig. 7 are calculated with an effective relaxation time of 30 ps, which is based on our experimental results discussed below. In this case a negligible shift of the maximum of the profiles can be observed with the reduction of the hole radius. Larger effective relaxation times and diffusivities, however, lead to a noticeable dependence of the effective rise time on the mask geometry. If we have long relaxation and exciton-formation times, some excitons can diffuse to masked parts before all carriers which have been generated by the laser pulse reach the $n=1$ exciton state. Hence, the shift is observed when the effective relaxation time and a characteristic transport time, given by the diffusion, reach the same order of magnitude (see Fig. 5). In addition, the transport effects may, e.g., lead to changes in the populations of the bands, which could accelerate the relaxation²² and may also contribute to such a shift.

V. EVALUATION OF TRANSPORT PARAMETERS BY LINE-SHAPE FITS

The theoretical profiles (Sec. IV) can be fitted to the experimental curves. This determines the diffusivity as the only fit parameter very sensitively, since the lifetimes are measured separately (Fig. 4). Figure 8 demonstrates the sensitivity of our method showing the concentration of excitons remaining in the hole area as a function of time. The dots represent the measured profile which is reproduced best by the theoretical curve (solid line) calculated for a diffusivity of $15 \text{ cm}^2/\text{s}$. Theoretical profiles calculated for the half and double value of D are also given in Fig. 8 and plotted as dotted and dashed lines, respectively.

The diffusivity in Eq. (1) does not depend on space. This can be verified by TOF studies carried out with holes of different radii as shown in Fig. 5. Figure 9 displays the diffusivities obtained by line-shape fits as a function of the hole radius for two different well widths. For a given temperature and a given well width, the evaluation yields the same value for the diffusivity within the experimental error for all different hole radii $\geq 1.5 \mu\text{m}$. This distinctly demonstrates the diffusive character of the motion over distances greater than $1.5 \mu\text{m}$ and the high utility of our TOF method.

Hence, the 2D exciton transport can be described by an isothermal diffusion [Eq. (1)] over distances greater than $1.5 \mu\text{m}$. This result is consistent with our studies on the transport processes in a 2D electron-hole plasma in GaAs/Ga_{1-x}Al_xAs QW's.¹⁶

The diffusivities obtained by the line-shape fits are shown in Fig. 10 as a function of temperature for a sample with a barrier-aluminum content of $x_{\text{Al}}=0.5$ containing QW's of $L_z=4, 8,$ and 15 nm . For comparison, results of an effectively 3D GaAs sample with $L_z=74 \text{ nm}$ are given. The diffusivities show a strong dependence on temperature, increasing up to about 100 K and decreasing

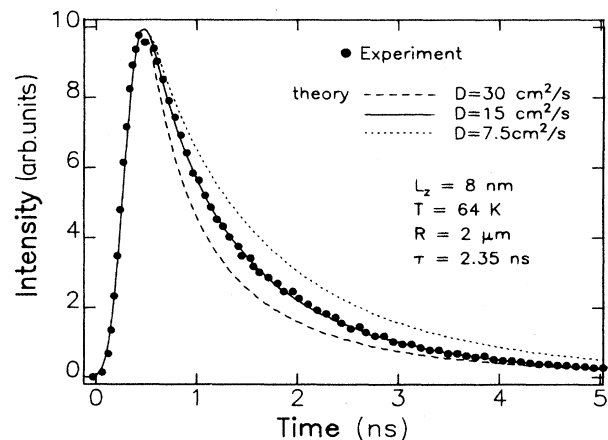


FIG. 8. Evaluation of an experimental profile (dots) by line-shape fits. Three theoretical profiles for different diffusivities are displayed by different line types. The best fit yields $D=15 \text{ cm}^2/\text{s}$.

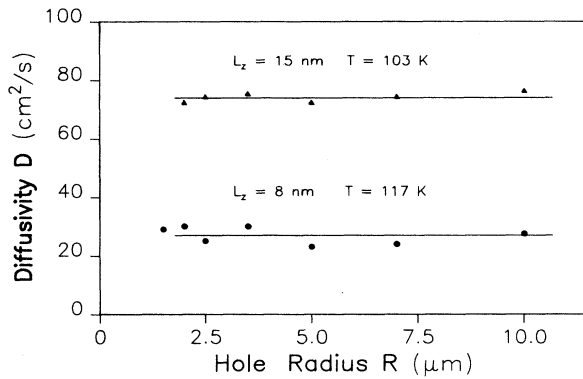


FIG. 9. Diffusivities of excitons confined in QW's of 8 and 15 nm well width obtained by line-shape fits for different hole radii.

ing again at higher temperature. In addition to this temperature dependence, a strong dependence on well width is observed. The diffusivities are reduced with decreasing L_z over the entire temperature range. This dependence on L_z is found to be rather weak at higher temperatures and very strong at low temperatures. A similar dependence on temperature and well width is further found in samples with $x_{Al}=1$ and in a sample with $x_{Al}=0.3$.

The decrease of the diffusivities with decreasing well width, which is observed here for the case of exciton transport in GaAs/Ga_{1-x}Al_xAs, is consistent with the results of a number of transport studies in other layered systems. For example, in Si:H and SiC:H (Ref. 15) a decrease of the 2D ambipolar diffusivity with decreasing layer thickness was reported. In GaSb/InAs QW's (Ref. 23) a similar behavior for 2D electrons was observed. Since the carrier concentration also changes with varying

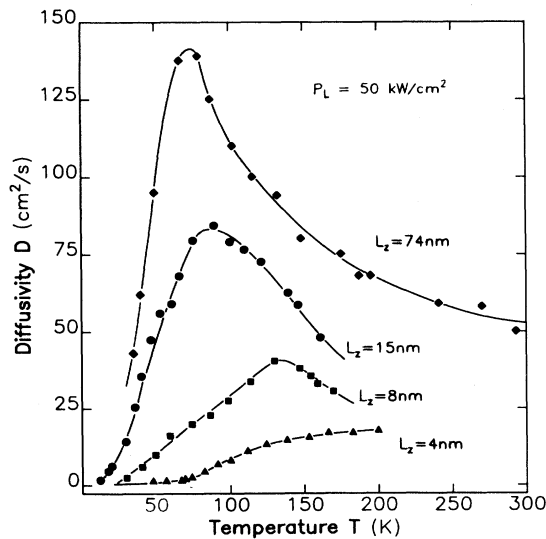


FIG. 10. Diffusivities as a function of temperature for three different QW widths and an aluminum mole fraction of 0.5 in comparison with a 3D GaAs layer of 74 nm width. The lines are drawn to guide the eye.

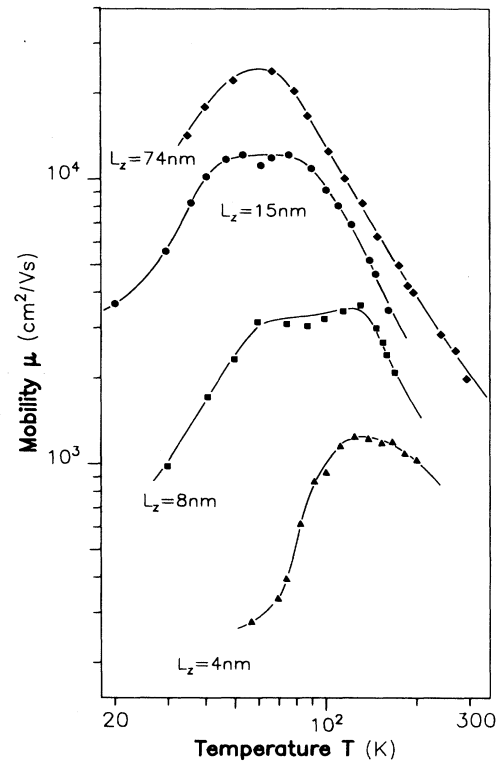


FIG. 11. Mobilities of excitons as a function of temperature and well width, obtained from the data of Fig. 10.

L_z during the latter experiment, a direct and quantitative correlation between the mobilities and the well widths is difficult in Ref. 23. In GaAs QW's a clear dependence of the electron Hall mobility on the well width was observed.^{7,8}

For low densities like those considered here, the conversion of the diffusivity as a function of temperature into the corresponding temperature-dependent mobility is possible using the density-independent Einstein relation $\mu(T) = D(T)e / (kT)$. For $x_{Al}=0.5$, the mobilities for different L_z are shown in Fig. 11 in a double-logarithmic plot as a function of temperature. For excitons in a 3D layer, a lateral mobility of about 2×10^4 cm²/V s is found for $T=80$ K. This can be compared with minority-carrier-mobility values published for liquid-nitrogen temperatures: about 2.2×10^5 cm²/V s for electrons^{24,25} and about 9500 cm²/V s for holes²⁶ for residual impurity densities in the range 10^{13} – 10^{14} cm⁻³. For the 2D exciton systems we find maximum mobilities of 12 200 cm²/V s for the 15-nm QW at $T=70$ K, 3600 cm²/V s for the 8-nm QW at 120 K, and 1240 cm²/V s for the 4-nm QW at 125 K. The solid line is drawn to guide the eye.

VI. EXCITON SCATTERING MECHANISMS

In this section the dependence of the mobility on temperature and on well width will be discussed. For that purpose the 3D and 2D transport is treated separately.

Figure 12 includes the measured 3D exciton mobility together with calculated mobility profiles as a function of

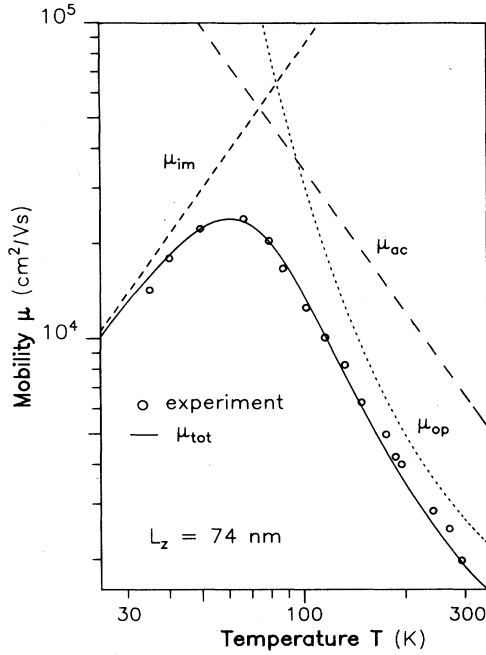


FIG. 12. Comparison of the measured mobility of 3D excitons (dots) as a function of temperature with calculated contributions of different scattering mechanisms (im denotes ionized impurity scattering, ac, acoustic-deformation-potential scattering and po, polar-optical scattering). The total mobility (solid line) is obtained by a fit including these scattering processes using Mathiessen's rule.

temperature. The experimentally observed exciton mobility (symbols) can be described very well by a fit which includes the contributions of three different scattering mechanisms:²⁷ scattering by ionized impurities, scattering by acoustic phonons via the deformation potential, and polar-optical scattering. The scattering rates of these contributions can be added using the Mathiessen rule to obtain the total scattering rate. This leads to a summation of different temperature dependences where an adjustable parameter accounts for the importance of each specific mechanism. These parameters are varied to fit the measured mobility data. The increasing branch of the mobility at low temperatures is due to scattering with ionized impurities, while the decreasing part at higher temperatures is due to scattering via the acoustic-deformation-potential and polar-optical scattering processes.

In the following we discuss 2D scattering processes which may cause the dependence on L_z observed experimentally. Mobility calculations for specific scattering mechanisms will be presented. These theoretical limits for the mobility are calculated for different scattering processes without any fit parameter.

The scattering of carriers via the acoustic deformation potential will be treated first. Two possible scattering cases are considered below and compared to the experiment to decide which of them describes the measurements.

(i) The ambipolar mobility. In this case two independent

particles (electron and hole) are considered. The mobility for each of these particles is given by

$$\mu_e = \frac{e}{m_{\text{opt},e,\parallel}} \langle \tau_e \rangle_E, \quad \mu_h = \frac{e}{m_{\text{opt},h,\parallel}} \langle \tau_h \rangle_E. \quad (2)$$

$\langle \rangle_E$ denotes an averaging over the energy, e the elementary charge, $m_{\text{opt},\parallel}$ the optical mass parallel to the interface, and τ the scattering time, which depends on the density-of-states mass. Due to the isotropic shape of the conduction band, the electron optical mass is equal to the electron density-of-states mass. In the valence band, the carrier confinement in 2D breaks the degeneracy of the heavy and light hole at the Γ point. The resulting energy splitting depends on the well width (e.g., 66, 22, and 10 meV for the 4-, 8-, and 15-nm QW, respectively). In the temperature range, where the acoustic-deformation-potential scattering is expected to dominate and for the carrier densities considered here, the occupation of the light-hole subband is negligible. Hence, in two dimensions, the optical mass and the density-of-states mass in the valence band are given by the heavy-hole mass m_{hh} .

The ambipolar mobility finally is given by

$$\mu_{\text{amb}} = \frac{2}{\mu_e^{-1} + \mu_h^{-1}}. \quad (3)$$

From expressions for 2D unipolar scattering times τ (Refs. 6 and 28) the corresponding ambipolar mobilities can be calculated using Eqs. (2) and (3). For the low carrier densities considered here an integral which occurs in the expression for the acoustic-deformation-potential scattering can be expanded. The differences between the 2D and 3D mobilities result mainly from the differences in the density of states. This leads to different power-law dependences on temperature and masses as well as to the additional dependence on the well width for the 2D system. The ambipolar mobility is found to be

$$\mu_{\text{ac,amb}} = \frac{2e\hbar^3 v_{\parallel}^2 \rho L_z}{(E_{d,e}^2 m_e^2 + E_{d,h}^2 m_{\text{hh},\parallel}^2) kT}. \quad (4)$$

In Table II the expressions used in Eq. (4) are explained and the corresponding values are given.

(ii) The mobility in the excitonic scattering condition. In this case the particle is scattered as a unit. For the scattering via the acoustic deformation potential, this is called the "hydrostatic scattering limit."¹⁹ In this case the excitonic deformation potential is given by

$$E_{d,\text{exc}} = E_{d,e} + E_{d,h}. \quad (5)$$

Due to the valence-band splitting at the Γ point and the differences in the density of states between these two bands, the light-hole band can also be neglected in this case. This means that 2D excitons are mainly heavy-hole excitons. The excitonic density-of-states mass and the excitonic optical mass are equal for that reason and are given by

$$M_{\parallel} = m_e + m_{\text{hh},\parallel}. \quad (6)$$

Using Eqs. (5) and (6), the mobility of excitons in the excitonic scattering condition via the acoustic deformation

TABLE II. Values of GaAs material parameters used in the calculations.

| | |
|----------------------------------|--|
| $m_e = 0.0665m_0$ | electron effective mass (Ref. 49) (used for 2D and 3D carrier systems) |
| $m_{1h} = 0.08m_0$ | light-hole effective mass (Ref. 49) (3D value) |
| $m_{1h} = 0.092m_0$ | light-hole effective mass (Refs. 45 and 46) (2D value) |
| $m_{hh} = 0.45m_0$ | heavy-hole effective mass (Ref. 49) (3D value) |
| $m_{hh,\perp} = 0.377m_0$ | heavy-hole effective mass (Refs. 45 and 46) (2D value) |
| $m_{hh,\parallel} = 0.2m_0$ | heavy-hole effective mass (Refs. 47 and 48) (2D value) |
| $v_l = 5.2 \times 10^5$ cm/s | velocity of longitudinal-acoustic phonons (Refs. 28 and 49) |
| $v_t = 2.99 \times 10^5$ cm/s | velocity of transversal-acoustic phonons (Refs. 28 and 49) |
| $E_{d,e} = 14$ eV | electron acoustic-deformation potential (Ref. 33) |
| $E_{d,h} = -3.5$ eV | hole acoustic-deformation potential (Ref. 49) |
| $\rho = 5.346$ g/cm ³ | mass density ($T = 100$ K) (Ref. 49) |
| $\epsilon_0 = 12.8$ | static dielectric permittivity (100 K) (Refs. 49 and 50) |
| $\epsilon_\infty = 10.9$ | high-frequency dielectric permittivity (Refs. 49 and 50) |
| $\hbar\omega_{LO} = 36.2$ meV | optical-phonon energy (Ref. 51) |
| $\Theta = 360$ K | Debye temperature (Refs. 49 and 27) |

potential is found to be

$$\mu_{ac,exc} = \frac{e\hbar^3 v_l^2 \rho L_z}{E_{d,exc}^2 M_{\parallel}^2 kT} \quad (7)$$

Figure 13 shows calculated mobilities for scattering via the acoustic deformation potential as a function of temperature for the excitonic and ambipolar conditions. The mobility for the ambipolar scattering condition is given by the dotted lines for three different well widths. The dependence of the mobility on temperature and well width (L_z/T) given by Eq. (4) can be seen directly. Figure 13 shows an increase of the mobilities by a factor of 10 when the temperature is reduced by 1 order of magni-

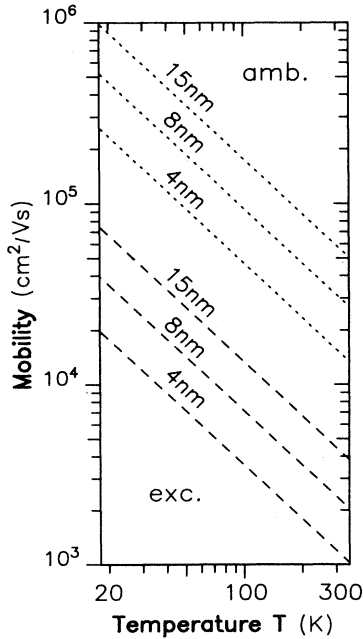


FIG. 13. Mobility limits for scattering via the acoustic deformation potential for QW widths of 4, 8, and 15 nm as a function of temperature. Mobilities calculated for the ambipolar condition (dotted lines, abbreviation amb.) and for the excitonic condition (dashed lines, abbreviation exc.) are displayed.

tude. The dashed line gives the adequate mobilities for the excitonic scattering condition which have the same dependence on T and L_z but are smaller by more than 1 order of magnitude than the results of the ambipolar calculation.

If we compare these theoretical data with our experimental results we find that the experiment can be described very well by the excitonic scattering condition (see Fig. 11). The ambipolar description, on the contrary, which considers two independent particles, leads to much higher mobilities than observed experimentally. This suggests the excitonic character of both the particles examined here and the scattering and transport process in the temperature range where the scattering by acoustic

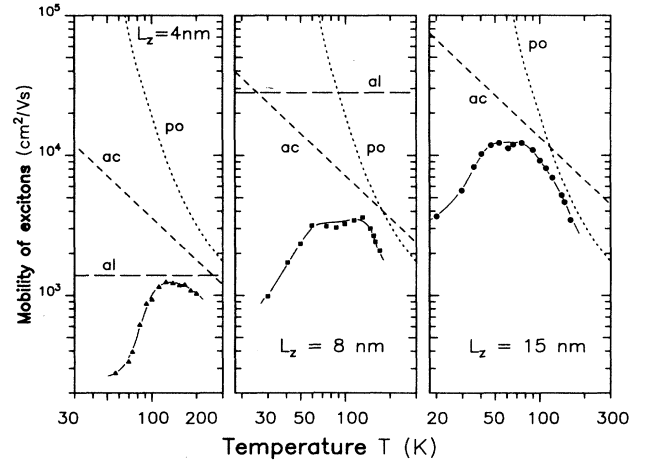


FIG. 14. The experimental and calculated mobility of 2D excitons (symbols) for three different well widths as a function of temperature are shown in three diagrams, one for each well width (subdiagrams a–c). At high temperature the measurements can be described well by mobility limits for acoustic-deformation-potential scattering (short-dashed lines), barrier-alloy scattering (long-dashed lines) and polar-optical scattering (dotted lines). The line-type abbreviations are po for polar-optical scattering, ac for acoustic-deformation-potential scattering, and al for barrier-alloy-disorder scattering. The strong well-width dependence at low temperatures is attributed to interface roughness scattering.

phonons via the deformation potential dominates. This excitonic scattering condition for acoustic-deformation-potential scattering was also found for exciton transport in Si (Ref. 19) in the relevant temperature range.

In Fig. 14, for each of the three QW widths a quantitative comparison is given in a separate diagram between the measured mobilities (symbols) and several calculated mobility limits as a function of temperature. Note that the plotted mobility range is the same for the three diagrams. The solid line connects the symbols and is drawn to guide the eye only. The scattering via the acoustic deformation potential is given by the short-dashed line and is indicated by "ac." In the temperature range where the acoustic-deformation-potential scattering dominates, we obtain a reasonable agreement between experiment and theory. Note that no fit parameter is included in the theory.

The mobility limit calculated for 2D piezoelectric scattering²⁸ is independent of the well width, which is in contradiction to the trend observed in the measured data. The influence of the piezoelectric scattering on the mobility of excitons is therefore expected to be negligible.

At higher temperatures, the measured mobilities decrease more strongly with increasing temperature than predicted by the limits of μ_{ac} . This deviation grows with increasing temperature and is due to polar-optical scattering becoming dominant in this temperature range. A proper theoretical treatment of polar-optical scattering is very difficult. Reported 2D mobility calculations²⁹ are discussed critically in Ref. 30. Since the deviations from 2D values are expected to be small,^{31,32} the 3D mobility is often used for the description of 2D electron transport.^{31,33} For the ambipolar case, in addition, the different coupling behavior between optical phonons and the *s*-like electrons or *p*-type holes has to be included. Because a proper treatment of 2D optical scattering has been proposed³⁰ but not performed to our best knowledge, we use the 3D mobility as a rough estimate. The dotted line in Fig. 14 represents the result of this estimate for the excitonic scattering condition. It should be noted, however, that the real 2D mobilities due to polar-optical scattering probably will have a dependence on the well width. This may lead to deviations from the estimate, mainly for small well widths. From Fig. 14(a) a small reduction of the polar-optical mobility with decreasing well width would be consistent with the experimental data.

For 2D carrier systems confined by ternary or quaternary barrier materials, another scattering mechanism can be important. Depending on the barrier height and the well width, a significant part of the wave functions of electrons and/or holes penetrates into the barrier. In the group-III sublattice, Al and Ga atoms are distributed randomly, which leads to a fluctuating potential, causing a scattering process in the alloy. Since in our case the scattering occurs only in the barriers, this process is called barrier-alloy-disorder scattering.³⁴ The penetration depth of the wave function is calculated using a QW model with finite barriers. For a fixed barrier height given by both the aluminum content *x* and the partition of the band discontinuity,^{35–38} and for a variable well

width as considered here, the penetration of the wave function is found to increase with decreasing well width. This is due to the growing quantization energy of the first subband, which reduces the effective barrier height.

In the Appendix, the calculation including one subband is described. The results of these calculations are shown in Fig. 14. The ambipolar mobility for the barrier-alloy-disorder scattering is given by the long-dashed lines. The value of the barrier-alloy-disorder mobility of the 15-nm QW is above the top line of Fig. 14(c) at a value of 6×10^5 cm²/V s. The calculated mobilities show a continuous rise with increasing well width ($L_z \geq 3$ nm) as observed experimentally. This directly reflects the decreasing penetration of the wave functions into the barriers. Except for the 4-nm QW, however, the absolute values of the barrier-alloy-disorder mobility limits are larger than observed in our experiment, which is equivalent to a smaller scattering probability. Hence, the barrier-alloy-disorder scattering seems to have less influence on the mobility for larger well widths. For smaller well widths (< 8 nm), however, the barrier-alloy-disorder scattering yields an upper limit for the mobility of excitons in the temperature range between 70 and 150 K. The dependence of the barrier-alloy-disorder scattering mobility on the temperature is extremely weak [see Figs. 14(a) and 14(b)] and is caused by the temperature dependence of the distribution functions of the initial and final states of the scattering process.

In contrast to the acoustic-deformation-potential scattering, a proper theoretical treatment of the alloy-disorder mobility for the excitonic scattering condition is very complicated. We estimate, however, that the result will be perhaps very similar to the calculated ambipolar condition, since the scattering process is due to the specific characters of the electrons and holes in the electron and hole potential wells, respectively. Therefore, the electrons and holes are expected to scatter separately. This is called a single-particle scattering condition, and is equivalent to the ambipolar scattering condition.

At low temperatures, the measured excitonic mobilities are strongly L_z dependent. From our experimental data we find $\mu \sim L_z^{2.5}$. Note that the exponent changes slightly when the contributions of the other scattering processes are included. We attribute the strong reduction of μ with decreasing L_z to scattering processes at roughnesses at the GaAs/Ga_{1-x}Al_xAs interface. Microscopic fluctuations of the well width in the lateral direction lead to fluctuations in the quantization energy which strongly increase with decreasing L_z . These fluctuations represent an additional scattering potential which dominates the transport properties at low temperatures, especially for small well widths. For 2D electrons, a strong reduction of the unipolar mobility due to interface roughness scattering was reported in theoretical³⁹ and experimental studies.^{7,8}

For low temperatures, the observed small diffusivities of the excitons confined in narrow QW's may also be influenced by localization effects. In the easiest model trapping and thermal reemission leads to a hopping-like motion, which can be described by small diffusivities as, e.g., those known from diffusion of impurities in semicon-

ductors.⁴⁰ Recently, localization effects have been investigated fundamentally.^{41–43,14} Experimentally, the localization of excitons in GaAs/Ga_{1-x}Al_xAs QW's was studied in detail at 5 K.¹⁴ A dependence of the diffusivities of excitons on their energy within the inhomogeneous line was reported, indicating a separation of the excitons into localized and nonlocalized excitons. The observed diffusivity of 15 cm²/s (Ref. 14) for nonlocalized excitons in a 21-nm QW at 5 K is in good agreement with extrapolations of our results. Diffusivity values for localized excitons were found to be near 1 cm²/Vs at 5 K.

Scattering at ionized impurities⁴⁴ cannot account for the observed strong mobility reduction at low temperatures. Indeed, μ_{im} increases linearly with growing temperature in two dimensions, which is similar to the measured behavior. However, the mobility is increasing with decreasing well width,⁴⁴ which is in contradiction to the experimental data shown in Fig. 14. Since the samples are not intentionally doped, the absolute values are well above the measured mobilities and do not influence the transport. Hence, ionized-impurity scattering and barrier-alloy-disorder scattering cannot describe the strong well-width dependence at low temperatures. This emphasizes the importance of interface roughness scattering for 2D excitons at low temperatures, which limits the mobility mainly for small QW's.

VII. CONCLUSIONS

We have presented results on lateral excitonic transport in 2D GaAs obtained by an all-optical TOF method. This method combines a high spatial resolution provided by microstructured masks, a high sensitivity given by the radial symmetry, and a high temporal resolution. The lateral motion of the 2D excitons can be described by an isothermal diffusion. A strong dependence of the mobility on temperature and well width was observed. In the higher-temperature range the results can be explained by polar-optical scattering, barrier-alloy-disorder scattering, and the acoustic-deformation-potential scattering in the excitonic scattering condition. At low temperatures, the importance of interface roughness scattering was pointed out. This mechanism is responsible for the observed strong decrease of the diffusivities with decreasing well width.

ACKNOWLEDGMENTS

The authors would like to thank M. H. Pilkuhn and T. Kuhn for stimulating discussions and R. Germann for the etching of the masks. The financial support by the Deutsche Forschungsgemeinschaft (Sonderforschungsbereich 329) and the Stiftung Volkswagenwerk is gratefully acknowledged.

APPENDIX

To calculate the influence of the barrier-alloy-disorder scattering which is due to the extension of the carrier wave function into the QW barrier, a symmetric finite QW of width L_z is considered. The band-edge discontinuities causing the electron and hole confinements are designated by ΔE_c and ΔE_v , respectively. In the following the subscript i denotes e for electrons and h for holes as used, e.g., for the barrier masses $m_{b,i}$ and the QW masses $m_{q,i}$. At the carrier densities considered here, only the lowest subband of each well is occupied and intersubband scattering can be neglected. In this case the z -dependent wave function in the barriers ($|z| > L_z/2$) is given by

$$\Psi_i^\pm(z) = \left[\frac{1}{\beta_i} + \frac{L_z/2}{\cos^2(\alpha_i L_z/2)} + \frac{m_{q,i}\beta_i}{m_{b,i}\alpha_i^2} \right]^{-0.5} \times \exp \left[\beta_i \left[\frac{L_z}{2} \pm z \right] \right]. \quad (\text{A1})$$

The abbreviations α_i and β_i contain the energy of the ground state E_i :

$$\alpha_i^2 = \frac{2m_{q,i}E_i}{\hbar^2}, \quad \beta_i^2 = \frac{2m_{b,i}(\Delta E_i - E_i)}{\hbar^2}. \quad (\text{A2})$$

The energy E_i is obtained from

$$m_{b,i}\alpha_i = m_{q,i}\beta_i \tan(\alpha_i L_z/2). \quad (\text{A3})$$

The rate for barrier-alloy-disorder scattering is calculated in the literature for various conditions using different approximations.^{6,29,34} We have calculated the scattering rate for one subband, neglecting screening effects and including the occupation function for the initial and final states of the scattering process. Including Eqs. (A1)–(A3)

TABLE III. Values of Ga_{1-x}Al_xAs material parameters used in the calculations.

| | |
|---|---|
| $a = (0.5645 + 0.00078x)$ nm | lattice constant (100 K) (Ref. 49) |
| $E_g^\Gamma(x) = (1.501 + 1.239x + 0.37x^2)$ eV | band-gap energy at the Γ point (100 K) (Refs. 52 and 49) |
| $m_{b,e}^\Gamma = 0.0665 + 0.0735x$ | electron effective mass (Refs. 49 and 53) |
| $m_{b,hh} = 0.377 + 0.253x$ | heavy-hole effective mass (Refs. 49 and 53) |
| $m_{b,lh}^\Gamma = 0.092 + 0.1x$ | light-hole effective mass (Refs. 49 and 53) |
| $V_{0,e} = 0.6$ eV | electron alloy-disorder-scattering potential (Ref. 34) |
| $V_{0,h} = 0.21$ eV | hole alloy-disorder scattering potential (Refs. 34 and 35) |
| $\Delta E_c / \Delta E_v = 65/35$ | partition of the band discontinuity between conduction and valence band (Refs. 35–38) |
| $r_0 = 0.44a$ | radius of the Wigner-Seitz Cell (Ref. 54) |

the scattering rate is given by

$$\tau^{-1} = \frac{\pi^2}{\hbar^3} n_0 m_{i,\parallel} V_{0,i}^2 2 \int_{L_z/2}^{\infty} |I(z_k)|^2 x(1-x) F(T) dz_k, \quad (\text{A4})$$

$$I(z_k) = \int_{-r_0}^{r_0} |\psi(z+z_k)|^2 (r_0^2 - z^2) dz. \quad (\text{A5})$$

In these formulas, $V_{0,i}$ denotes the alloy-disorder scattering potential, n_0 the number of arsenic atoms per volume ($n_0 = 4/a^3$), x the aluminum content, and r_0 the radius of the Wigner-Seitz cell. The factor F describes a correction to Eq. (A4) if the distribution function of the final state is included in the integration. The density range considered here, however, leads to values for the factor F which are only somewhat larger than 1. The corresponding values are given in Tables II and III. For a comparison with the measurement, the dependences on the well width and the aluminum mole fraction x are of great interest. The aluminum mole fraction is included in n_0 , $m_{b,i}$, E_i , and the expression $x(1-x)$. The parameters α_i and β_i depend on the well width.

The ambipolar mobility limit can be calculated using Eqs. (2) and (3). The ambipolar mobility is found to in-

crease continuously with growing aluminum content x , for a constant well width and $x > 0.3$. This is due to the contribution of all these quantities, which depend on the mole fraction, as listed above. With growing aluminum content, the band-edge discontinuity increases, which leads to a decrease of the wave-function penetration into the barrier alloy. This dominates the dependence of the mobility on the aluminum mole fraction. For small x it even overcompensates for the dependence $[x(1-x)]^{-1}$ which is included in the mobility. In a 3D alloy, however, the alloy-disorder scattering process yields a dependence on x , which is rather similar to $[x(1-x)]^{-1}$, modified only by the x dependence of the masses and the specific character of the atoms which the alloy consists of.

Note that the "one-subband approximation" leads to deviations for large well widths (≥ 15 nm), since the subband separation is reduced with increasing well width. Due to the participation of higher subbands, the carrier system is no longer exactly 2D. Note further that the results are extremely sensitive to the partition of the band discontinuity between the conduction band and the valence band. The exact ratio for this partition is still a point of discussion even in the well-examined GaAs/Ga_{1-x}Al_xAs system.

*Permanent address: Nagaoka Technical College, Department of Electrical Engineering, Nagaoka 940, Japan.

¹J. H. English, A. C. Gossard, W. Wiegmann, R. Bondal, and K. Baldwin, *Appl. Phys. Lett.* **50**, 1826 (1987).

²G. Weimann, in *Festkörperprobleme (Advances in Solid State Physics)*, edited by J. Treusch (Vieweg, Braunschweig, 1986), Vol. XXVI.

³J. J. Harris, C. T. Foxon, K. W. J. Barnham, D. E. Lacklison, J. Hewitt, and C. White, *J. Appl. Phys.* **61**, 1219 (1987).

⁴E. E. Mendez, P. J. Price, and M. Heiblum, *Appl. Phys. Lett.* **45**, 294 (1984).

⁵H. J. Störmer, A. C. Gossard, W. Wiegmann, R. Bondal, and K. Baldwin, *Appl. Phys. Lett.* **44**, 139 (1984).

⁶C. Guillemot, M. Baudet, M. Gauneau, A. Regreny, and J. A. Portal, *Phys. Rev. B* **35**, 2799 (1987).

⁷H. Sakaki, T. Noda, K. Hirakawa, M. Tanaka, and T. Matsusue, *Appl. Phys. Lett.* **51**, 1934 (1987).

⁸R. Gottinger, A. Gold, G. Abstreiter, G. Weimann, and W. Schlapp, *Europhys. Lett.* **6**, 183 (1988).

⁹J. Degani, R. F. Leheny, R. E. Nahory, and J. P. Heritage, *Appl. Phys. Lett.* **39**, 569 (1981).

¹⁰M. Gallant and A. Zemel, *Appl. Phys. Lett.* **52**, 1686 (1988).

¹¹D. F. Nelson, J. A. Cooper, and A. R. Tretola, *Appl. Phys. Lett.* **41**, 857 (1982).

¹²R. A. Höpfel, J. Shah, P. A. Wolff, and A. C. Gossard, *Phys. Rev. B* **37**, 6941 (1988).

¹³B. Deveaud, J. Shah, T. C. Damen, B. Lambert, and A. Regreny, *Phys. Rev. Lett.* **58**, 2582 (1987).

¹⁴J. Hegarty and M. D. Sturge, *J. Opt. Soc. Am. B* **2**, 1143 (1985).

¹⁵K. Hattori, T. Mori, H. Okamoto, and Y. Hamakawa, *Appl. Phys. Lett.* **51**, 1259 (1987).

¹⁶H. Hillmer, A. Forchel, S. Hansmann, E. Lopez, and G. Weimann, *Solid-State Electron.* **31**, 485 (1988).

¹⁷K. T. Tsen and H. Morkoç, *Phys. Rev. B* **34**, 6018 (1986).

¹⁸H. Hillmer, S. Hansmann, A. Forchel, M. Morohashi, E. Lopez, H. P. Meier, and K. Ploog, *Appl. Phys. Lett.* **53**, 1937 (1988).

¹⁹G. Mahler, T. Kuhn, A. Forchel, and H. Hillmer, in *Optical Nonlinearities and Instabilities in Semiconductors*, edited by H. Haug (Academic, San Diego, 1988), p. 159.

²⁰H. Hillmer, G. Mayer, A. Forchel, K. S. Löchner, and E. Bauser, *Appl. Phys. Lett.* **49**, 948 (1986).

²¹J. Feldmann, G. Peter, E. O. Göbel, P. Dawson, K. Moore, C. Foxon, and R. J. Elliott, *Phys. Rev. Lett.* **59**, 2337 (1987).

²²H. Hillmer, A. Forchel, S. Hansmann, H. P. Meier, and K. Ploog (unpublished).

²³H. Munekata, E. E. Mendez, Y. Iye, and L. Esaki, *Surf. Sci.* **174**, 449 (1986).

²⁴H. Miki and M. Otsubo, *J. Appl. Phys.* **10**, 509 (1971).

²⁵L. Lin, Y. Lin, X. Zhong, Y. Zhang, and H. Li, *J. Cryst. Growth* **56**, 344 (1982).

²⁶K. H. Zschauer, in *Proceedings of the 4th International Symposium on GaAs and Related Compounds (1972)* (The Institute of Physics and Physical Society, London, 1973), p. 6.

²⁷B. R. Nag, in *Electron Transport in Compound Semiconductors*, Vol. 11 of *Springer Series in Solid-State Sciences*, edited by H.-J. Queisser (Springer, Berlin, 1980).

²⁸K. Lee, M. S. Shur, T. J. Drummond, and H. Morkoç, *J. Appl. Phys.* **54**, 6432 (1983).

²⁹B. J. F. Lin, D. C. Tsui, M. A. Paalanen, and A. C. Gossard, *Appl. Phys. Lett.* **45**, 695 (1984).

³⁰P. J. Price, *Phys. Rev. B* **32**, 2643 (1985).

³¹K. Hess, *Appl. Phys. Lett.* **35**, 484 (1979).

³²W. Walukiewicz, H. E. Ruda, J. Lagowski, and H. C. Gatos, *Phys. Rev. B* **30**, 4571 (1984).

³³An empirical temperature dependence $AT^{-2} + BT^{-6}$ deduced from 3D GaAs including the free parameters A and B is used

- in Ref. 28 to fit the 2D data.
- ³⁴S. B. Ogale and A. Madhukar, *J. Appl. Phys.* **56**, 368 (1984).
In this paper the mobility of electrons is calculated for a partition of the band discontinuity of 85/15.
- ³⁵H. Kroemer, Supplement of the Workbook, 2nd International Conference on Modulated Semiconductor Structures, 1985, p. 797 (unpublished).
- ³⁶R. C. Miller, D. A. Kleinman, and A. C. Gossard, *Phys. Rev. B* **29**, 7085 (1984).
- ³⁷P. Dawson, K. J. Moore, and C. T. Foxon, *Proc. SPIE* **792**, 208 (1987).
- ³⁸J. Menéndez, A. Pinczuk, D. J. Werder, A. C. Gossard, and J. A. English, *Phys. Rev. B* **33**, 8863 (1986).
- ³⁹A. Gold, *Z. Phys. B* **74**, 53 (1989).
- ⁴⁰D. L. Kendall and D. B. De Vries, in *Semiconductor Silicon*, edited by R. R. Haberecht and E. L. Kern (Electrochemical Society, New York, 1969), p. 358.
- ⁴¹N. F. Mott and E. A. Davis, *Electronic Processes in Noncrystalline Materials*, 2nd ed. (Clarendon, Oxford, 1979).
- ⁴²P. W. Anderson, *Physica B+C* **117&118B**, 30 (1983).
- ⁴³M. H. Cohen, H. Fritzsche, and S. R. Ovshinsky, *Phys. Rev. Lett.* **22**, 1065 (1969).
- ⁴⁴S. B. Ogale and A. Madhukar, *J. Appl. Phys.* **55**, 483 (1984).
- ⁴⁵R. C. Miller, D. A. Kleinman, and A. C. Gossard, *Phys. Rev. B* **29**, 7085 (1984).
- ⁴⁶U. Rössler, *Solid State Commun.* **65**, 1279 (1988).
- ⁴⁷D. A. Kleinman, *Phys. Rev. B* **28**, 871 (1983).
- ⁴⁸M. A. Gell, M. Jaros, and D. H. Herbert, *Superlatt. Microstruct.* **3**, 121 (1987).
- ⁴⁹*Physics of Group IV Elements and III-V Compounds*, Pt. a of *Semiconductors*, Vol. 17 of *Crystal and Solid State Physics*, Gp. III of *Landolt-Börnstein, Numerical Data and Functional Relationships in Science and Technology*, New Series, edited by K. H. Hellwege (Springer, Berlin, 1982); Vol. 22, *Intrinsic Properties of Group IV Elements and III-V, II-VI and I-VII Compounds* (edited by O. Madelung) (Springer, Berlin, 1987), pp. 218, 222–224, 234, and 247.
- ⁵⁰D. L. Rode, in *Semiconductors and Semimetals*, edited by R. K. Willardson and A. C. Beer (Academic, New York, 1975), Vol. 10, Chap. 1.
- ⁵¹M. Matsuura, *Phys. Rev. B* **37**, 6977 (1988).
- ⁵²S.-H. Wei and A. Zunger, *J. Appl. Phys.* **63**, 5794 (1988).
- ⁵³S. Adachi, *J. Appl. Phys.* **58**, R1 (1985).
- ⁵⁴J. W. Harrison and J. R. Hauser, *Phys. Rev. B* **13**, 5347 (1976).